Open access • Journal Article • DOI:10.1126/SCIENCE.AAD3345

On-chip and freestanding elastic carbon films for micro-supercapacitors

— Source link ⬈

Peihua Huang, Peihua Huang, Christophe Lethien, Christophe Lethien ...+19 more authors

Institutions: Centre national de la recherche scientifique, Paul Sabatier University, university of lille, Institut national des sciences appliquées ...+3 more institutions

Topics: Square Centimeter, Carbon film, Supercapacitor, Microfabrication and Silicon

Related papers:

- Ultrahigh-power micrometre-sized supercapacitors based on onion-like carbon

- Scalable fabrication of high-power graphene micro-supercapacitors for flexible and on-chip energy storage

- Capacitive energy storage in micro-scale devices: recent advances in design and fabrication of micro-supercapacitors

- Materials for electrochemical capacitors

- Laser Scribing of High-Performance and Flexible Graphene-Based Electrochemical Capacitors

22. G. D. Gilliland et al., Phys. Rev. Lett. **71**, 3717–3720 (1993).
23. D. Xiao, G. B. Liu, W. Feng, X. Xu, W. Yao, Phys. Rev. Lett. **108**, 196802 (2012).
24. W.-T. Hsu et al., ACS Nano **8**, 2951–2958 (2014).
25. A. M. van der Zande et al., Nano Lett. **14**, 3869–3875 (2014).
26. K. Liu et al., Nat. Commun. **5**, 4966 (2014).
27. H. Yu, Y. Wang, Q. Tong, X. Xu, W. Yao, Phys. Rev. Lett. **115**, 187002 (2015).
28. T. Cao et al., Nat. Commun. **3**, 887 (2012).
29. K. F. Mak, K. He, J. Shan, T. F. Heinz, Nat. Nanotechnol. **7**, 494–498 (2012).
30. H. Zeng, J. Dai, W. Yao, D. Xiao, X. Cui, Nat. Nanotechnol. **7**, 490–493 (2012).
31. M. M. Fogler, L. V. Butov, K. S. Novoselov, Nat. Commun. **5**, 4555 (2014).
32. P. J. Zomer, M. H. D. Guimarães, J. C. Brant, N. Tombros, B. J. van Wees, Appl. Phys. Lett. **105**, 013101 (2014).
33. Materials and methods are available as supplementary materials on Science Online.
34. C. Mai et al., Nano Lett. **14**, 202–206 (2014).
35. Q. Wang et al., ACS Nano **7**, 11087–11093 (2013).
36. C. R. Zhu et al., Phys. Rev. B **90**, 161302 (2014).

On-chip and freestanding elastic carbon films for micro-supercapacitors

P. Huang,[1,2] C. Lethien,[2,3] S. Pinaud,[4] K. Brousse,[1,2] R. Laloo,[1,2] V. Turq,[1,2] M. Respaud,[4,5] A. Demortière,[2,6] B. Daffos,[1,2] P. L. Taberna,[1,2] B. Chaudret,[4] Y. Gogotsi,[7] P. Simon[1,2]*

Integration of electrochemical capacitors with silicon-based electronics is a major challenge, limiting energy storage on a chip. We describe a wafer-scale process for manufacturing strongly adhering carbide-derived carbon films and interdigitated micro-supercapacitors with embedded titanium carbide current collectors, fully compatible with current microfabrication and silicon-based device technology. Capacitance of those films reaches 410 farads per cubic centimeter/200 millifarads per square centimeter in aqueous electrolyte and 170 farads per cubic centimeter/85 millifarads per square centimeter in organic electrolyte. We also demonstrate preparation of self-supported, mechanically stable, micrometer-thick porous carbon films with a Young's modulus of 14.5 gigapascals, with the possibility of further transfer onto flexible substrates. These materials are interesting for applications in structural energy storage, tribology, and gas separation.

T he plethora of portable electronic devices and the continued expansion of electronics into new mobile applications highlight the need for high-performance miniaturized electrochemical storage devices able to deliver energy from their environment. Radio frequency identification (RFID) tags for the development of smart environments are another critical application that requires compact energy storage. Accordingly, designing efficient miniaturized energy storage devices for energy delivery or harvesting with high-power capabilities remains a challenge (1).

Electrochemical double-layer capacitors (EDLCs), also known as supercapacitors, store the charge through reversible ion adsorption at the surface of high-surface-area carbons. Aside from an outstanding cycle life, this electrostatic charge storage results in devices with medium energy density (~6 W·h kg^{-1}) and high power densities (>10 kW kg^{-1}). As a result, supercapacitors complement—or can even sometimes replace—batteries in applications from electronics to public transportation and renewable energy stor-age, in which high-power delivery and uptake and very long cycle life are required (2).

A large variety of materials such as graphene (3–5), nanotubes (6, 7), carbide-derived carbons (CDC) (8, 9), and pseudocapacitive materials (1, 10, 11) have been explored in micro-supercapacitors in the past 5 years. Much of the recent work focused on the use of wet processing routes (using colloidal solutions or suspensions of particles for the electrode preparation) for the development of flexible micro-devices for printable electronics (1, 4, 5, 12). However, the wet processing methods are not fully compatible with semiconductor device manufacturing used in the electronics industry, thus hampering supercapacitor manufacturing on silicon chips. Vapor phase methods, such as atomic layer deposition, are limited to the preparation of thin layers of active materials, limiting the areal energy and power performance of the electrodes (13, 14). Direct growth of graphene or carbon nanotubes on a Si wafer results in low-energy-density devices (15). The pioneering concept of laser scribing of graphene developed by Kaner's group for preparing flex-ible micro-supercapacitors has shown outstanding power performance but fails to achieve high areal capacitance (< 5 mF cm^{-2}) (3, 5). Another strategy is to use pseudocapacitive materials, which have a larger capacitance, but moving from pure double-layer to pseudocapacitive charge storage comes with disadvantages, such as a decrease in power capabilities and cycle life because of the kinetic limitations of the redox reactions (10, 11, 16–20). Bulk CDC films (8, 9, 21) have shown high capacitance and high areal and volumetric energy density but poor integrity of the film from cracking and delamination (9).

To produce carbon films, TiC coatings of several micrometers in thickness were deposited by using a direct current magnetron sputtering (DC-MS) technique (supplementary materials, materials and methods). Shown in fig. S1A is a cross section of a 6.3-μm-thick TiC film deposited onto a SiO$_2$-coated Si wafer, by using the DC-MS technique. The resistivity, thickness, and mechanical stress of the TiC film can be fine-tuned by changing the deposition parameters (fig. S1, B and C). The film thickness changes linearly with the deposition time (fig. S1D), and films up to 20 μm thick could be prepared, with controlled roughness (fig. S1E). Samples were placed in a furnace and chlorinated at 450°C, thus transforming

[1]Université Paul Sabatier-Toulouse III, Laboratoire Centre Inter-universitaire de Recherche et d'Ingénierie des Matériaux (CIRIMAT), UMR CNRS 5085, 118 route de Narbonne, 31062 Toulouse, France. [2]Réseau sur le Stockage Electrochimique de l'Energie, FR CNRS n°3459, France. [3]Université Lille 1 Sciences et Technologies, Laboratoire Institut d'Electronique de Microélectronique et de Nanotechnologie (IEMN), UMR CNRS 8520, Cité scientifique, Avenue Henri Poincaré, CS 60069, 59652 Villeneuve d'Ascq cedex, France. [4]Laboratoire de Physique et Chimie des Nano-Objets (LPCNO), UMR 5215 Institut National des Sciences Appliquées (INSA)–Université Paul Sabatier (UPS)–CNRS, Université de Toulouse, INSA, 135 Avenue de Rangueil, 31077 Toulouse, France. [5]Atelier Interuniversitaire de Micro-nano Électronique (AIME), Université de Toulouse, INSA, UPS, INP, 135 avenue de Rangueil, 31077 Toulouse Cedex 4, France. [6]Laboratoire de Chimie et de Réactivité des Solides, UMR CNRS 7314, Université de Picardie Jules Verne, 80039 Amiens, France. [7]Department of Materials Science and Engineering, and A. J. Drexel Nanomaterials Institute, Drexel University, 3141 Chestnut Street, Philadelphia, PA 19104, USA.
*Corresponding author. E-mail: simon@chimie.ups-tlse.fr

the TiC film into CDC (8, 9, 21, 22) with a growth rate of 1 μm/min (table S2) by the reaction

$$TiC + 2Cl_2 \rightarrow TiCl_4 + C \qquad (1)$$

The chlorination time t_1 was fixed at 5 min for achieving a partial chlorination of the TiC layer, as shown in Fig. 1A, top. Shown in Fig. 1B is a cross section of the SiO_2 (Fig. 1B, bottom)/TiC (Fig. 1B, middle)/porous CDC structure. The thickness of the CDC layer was ~5 μm, so that a ~1.3-μm-thick film of metallically conducting TiC remained under the CDC layer.

Because of the partial chlorination, the transformation of TiC into porous CDC was, for the first time, achieved without any film delamination at either the CDC/TiC or TiC/SiO₂ interface. The presence of the ~1-μm-thick underlayer of TiC keeps the TiC/SiO₂ interface identical to the one observed before chlorination, with no trace of delamination or cracks.

Last, this TiC layer not only acts as a buffer and adhesion layer that accommodates the mechanical stresses between the Si wafer and the porous CDC but also can be used as a current collector because the electrical conductivity was kept above 10^3 S cm^{-1} (table S1).

Raman spectra of the TiC film before (Fig. 1C, red) and after (Fig. 1C, blue) chlorination were recorded. Peaks in the 250 to 750 nm range are shown in Fig. 1C, namely 250 cm^{-1}, 433 cm^{-1}, and 608 cm^{-1}, which are attributed to the TiC (23). The peaks completely disappeared after chlorination, and only the D and G bands of graphitic carbon, fairly typical for TiC-CDC (8, 21), were visible, thus confirming that Ti was removed during chlorination.

We measured the pore volume and the pore size distribution (Fig. 1D) using Ar and CO₂ gas sorption. The type 1 Ar adsorption isotherm (fig. S2A) shows a microporous sample, with all adsorption occurring at low pressures. The Brunauer-Emmett-Teller (BET) surface area was calculated at 977 ± 30 m^2 g^{-1}. CO₂ gas sorption measurements (fig. S2B) gave a micropore volume of 0.47 cm^3 g^{-1} and a very narrow pore size distribution (Fig. 1D), with a mean pore size of 0.59 nm and no pores larger than 1 nm. This zeolite-like pore size distribution confirms a very uniform structure of the film.

The transmission electron microscopy (TEM) investigation (Fig. 2) of a thin cross-sectional sample prepared with the focused ion beam (FIB) technique revealed a rugged interface, with sharp

needles of TiC penetrating into the carbon layer and providing excellent adhesion (Fig. 2, A to F). CDC shown in Fig. 2, G and H, was analyzed by means of high-angle annular dark-field scanning TEM (HAADF-STEM), and the estimated roughness and porosity of the surface were less than 1 nm.

The electrochemical characterization of the TiC/CDC films on Si wafers was performed in aqueous (1 M H₂SO₄) and organic (1 M EMI, BF₄ in acetonitrile) electrolytes in three-electrode cells. After chlorination, the samples were annealed under vacuum at 600°C for 2 hours so as to remove trapped chlorine and chlorides, as evidenced with Auger spectroscopy (fig. S3B). Cyclic voltammograms of a CDC sample in 1 M H₂SO₄ electrolyte, at 20 and 1 mV s^{-1} (Fig. 3A), have a rectangular shape typical for capacitive behavior. The slight current increase at negative potentials during negative sweep below –0.5 V versus Hg₂SO₄/Hg is assumed to originate from the pseudocapacitive contribution of proton reduction in confined carbon micropores, as proposed by Béguin et al. (24). The gravimetric capacitance is meaningless for microdevices (25); therefore, values of 410 F cm^{-3} and 205 mF cm^{-2} were calculated at 1 mV s^{-1} for the volumetric and
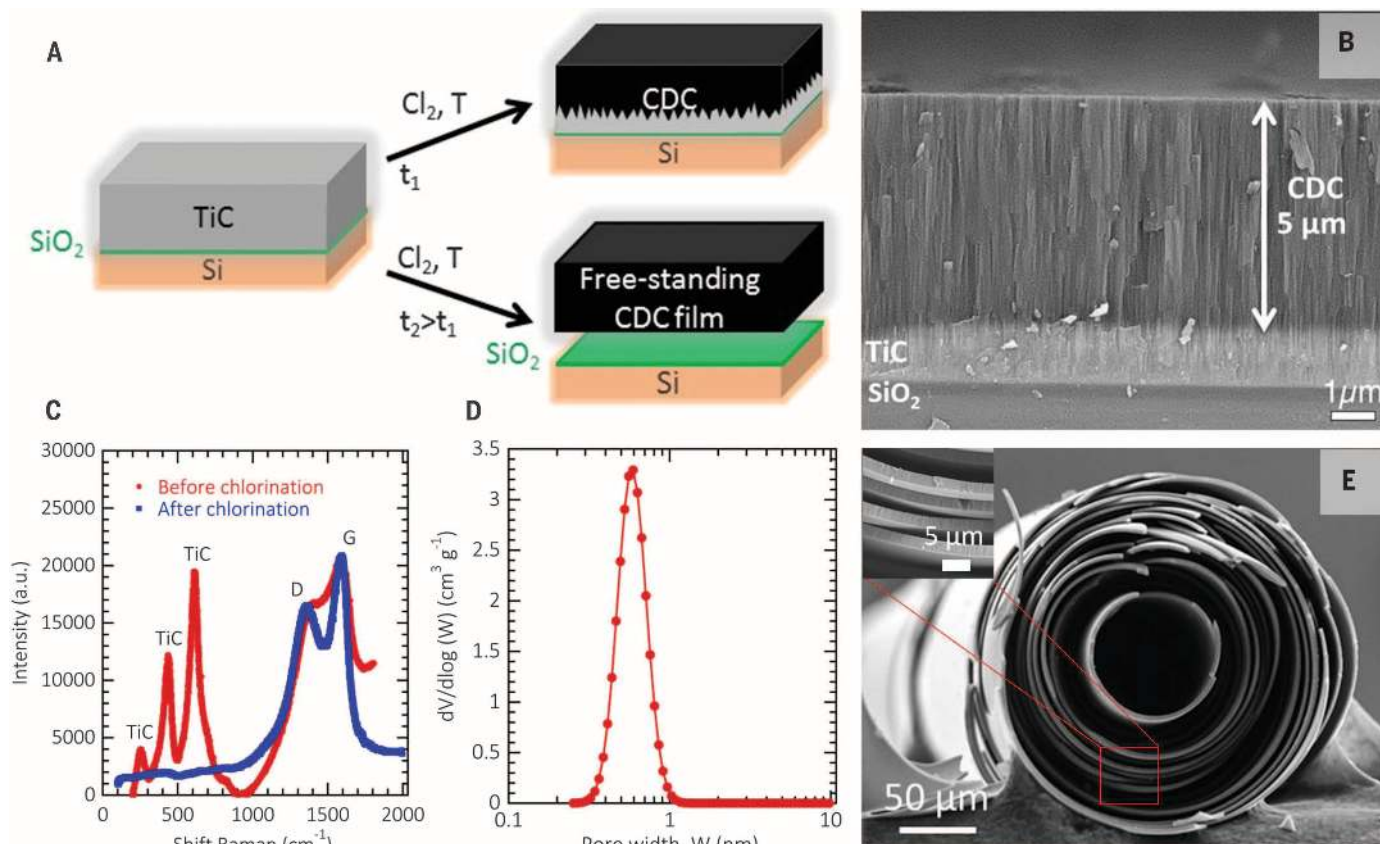

Fig. 1. Preparation of the microporous carbon films. (**A**) Scheme of the chlorination process. Starting from TiC films deposited onto a Si wafer, the partial chlorination of the films leads to SiO₂/TiC/CDC layered structures (top right). The full chlorination allows the synthesis of freestanding CDC films (bottom right). (**B**) SiO₂/TiC/CDC layered structures obtained after chlorination for 5 min at 450°C. (**C**) Raman spectra of the TiC and the CDC layers. (**D**) Pore size distribution of the porous CDC films from CO₂ gas sorption, using the Reverse Monte Carlo model. The isotherm shows a microporous sample, with an estimated average pore size of 0.59 nm. (**E**) Cross-sectional SEM images of rolled freestanding delaminated films obtained through full chlorination.

areal capacitance, respectively. Cyclic voltammetry at low scan rates provides evidence of a low-leakage current in the cell. The electrode capacitance was stable over 10,000 cycles (Fig. 3B). The change of the normalized capacitance versus the potential scan rate provides evidence for the high power capability of these films (Fig. 3B, inset) as more than 200 F cm^{-3} (100 mF cm^{-2}) were still delivered during 0.9 s discharge (1 V s^{-1}), which outperforms the current state of the art of carbon-based double-layer capacitors and micro-supercapacitors (26–30).

The cyclic voltammogram (CV) of a Si/TiC/CDC film annealed at 600°C in hydrogen and tested as a single electrode at 20 mV s^{-1} in 1 M EMI,BF$_4$ in acetonitrile electrolyte shows a typical capacitive behavior within a potential window limited to 2.0 V (fig. S3D). The volumetric capacitance of the sample reached 170 F cm^{-3}, which is in line with the data reported for TiC-CDC films (8). Annealing at 600°C under H$_2$

atmosphere opens carbon pores (22), thus improving accessibility to large EMI$^+$ ions compared with that of a nonannealed sample (fig. S3C) without affecting the adherence at the CDC/TiC interface. CDC pore size, which determines capacitance, can be controlled with the synthesis temperature (8, 21, 22). Shown in Fig. 3C are CVs of a 2.2-μm-thick CDC film on a Si/TiC/CDC electrode prepared through partial chlorination at 700°C for 30 s, obtained at different rates. CVs show a typical capacitive behavior within a potential window up to 3 V, resulting in an improvement of the energy and power density (Fig. 4) and the volumetric capacitance reaching 160 F cm^{-3} at 20 mV s^{-1}.

Following the electrochemical characterizations of the CDC films, two-electrode micro-supercapacitor devices were manufactured and characterized. Micro-supercapacitors containing nine fingers per polarity (2 mm long, 100 μm wide, with 15 μm separation) (Fig. 3D) were prepared

according to the different steps detailed in figs. S4 and S5, A to C. A picture of a 7.62-cm Si wafer containing 40 patterned micro-supercapacitors is shown in Fig. 3E, thus confirming that the process can be easily scalable. Ti/Au film was evaporated on both sides of the large pad for ensuring electrical contact. The CVs of a micro-supercapacitor in H$_2$SO$_4$ 1 M electrolyte are presented in Fig. 3F. In this example, the chlorination of a 3.5-μm-thick patterned TiC layer led to formation of a 1.4-μm-thick CDC film. The electrode volumetric capacitance reached 350 F cm^{-3}, which is in line with the electrochemical performance of three-electrode cells presented in Fig. 3A. The slight decrease of the volumetric capacitance compared with that of a single electrode (410 F cm^{-3}) may originate from very small separation (only 15 μm) between the electrode fingers. The capacitance change with the potential scan rate is shown in fig. S5D; the initial capacitance is 350 F cm^{-3}. More than 50%
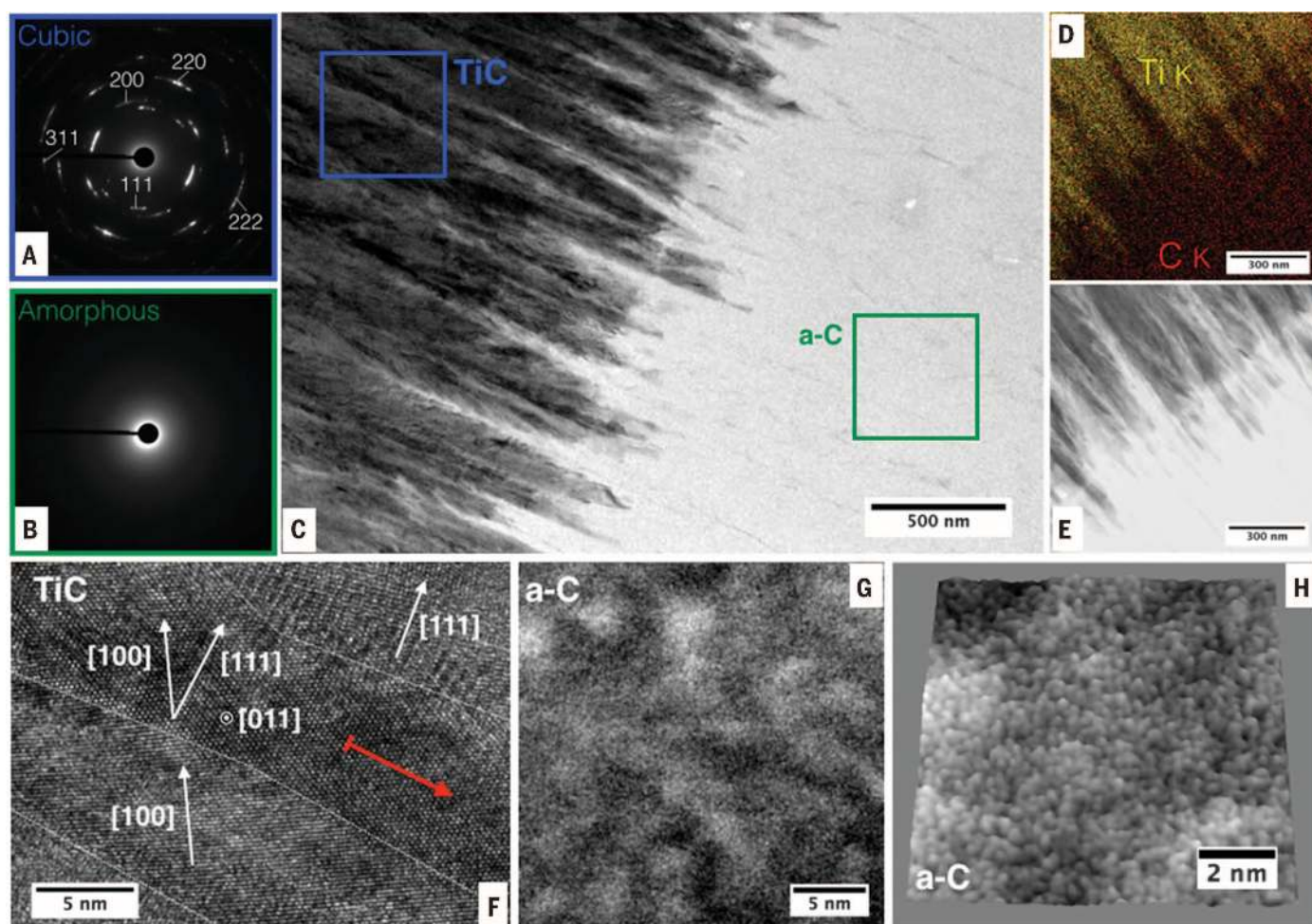

Fig. 2. Structural characterization of the SiO$_2$/TiC/CDC electrodes. (**A**) Selected-area electron diffraction (SAED) pattern of TiC [(C), blue square] showing the cubic structure. (**B**) SAED pattern of CDC [(C), green square], showing an amorphous structure. (**C**) TEM image of the TiC/CDC interface, with the areas for the SAED analysis [blue and green squares in (A) and (B), respectively]. (**D**) Energy-dispersive x-ray analysis showing the absence of Ti in the carbon film. (**E**) Bright-field STEM image of the interface, showing the interpenetration of TiC and carbon structures, which proves the excellent adhesion between the layers. (**F**) High-resolution TEM image showing the crystallographic orientation of the TiC cubic structure. (**G**) HAADF-STEM image of the amorphous carbon and (**H**) roughness of the CDC surface, which is estimated to be less than 1 nm (scanned area, 10 by 10 nm).
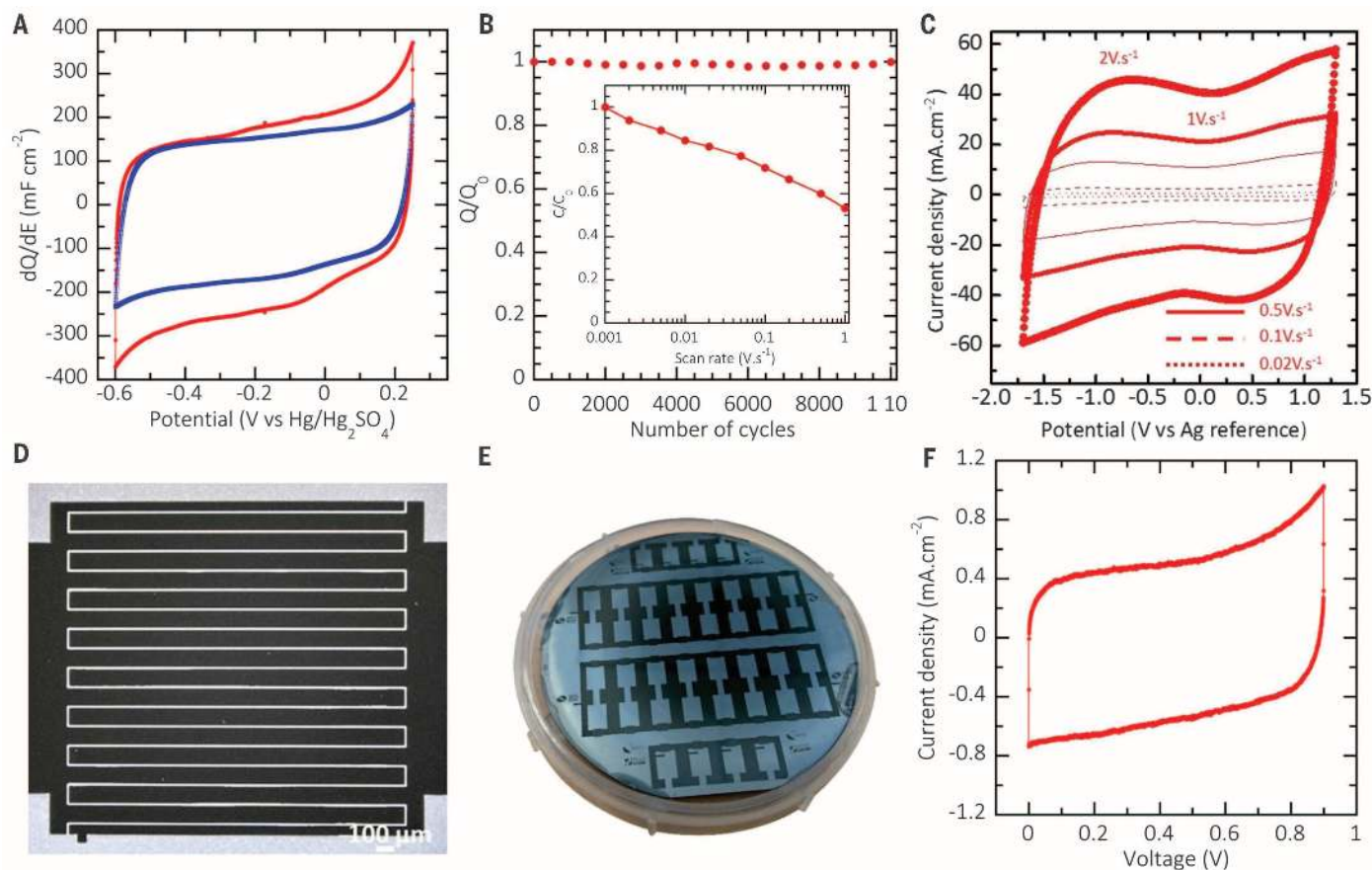
Fig. 3. Electrochemical characterizations. (**A**) CVs of a Si/TiC/CDC electrode in 1 M H_2SO_4 electrolyte at 20 mV s^{-1} (blue curve) and 1 mV s^{-1} (red curve), both after annealing 2 hours at 600°C under vacuum. The volumetric capacitance reaches 410 F cm^{-3} or 205 mF cm^{-2}. (**B**) No capacitance loss was observed up to 10,000 cycles. (Inset) Change of the normalized capacitance with the potential scan rate for a 5-μm-thick CDC sample. The initial value is 410 F cm^{-3} (205 mF cm^{-2}). (**C**) CVs of a SiO$_2$/TiC/CDC electrode (2.2-μm-thick CDC film), which was chlorinated at 700°C and annealed in H_2 for 1 hour at 600°C, in 2 M EMI,BF$_4$ in CH$_3$CN electrolyte at various scan rates. The volumetric capacitance reaches 160 F cm^{-3} within a 3-V potential window. (**D**) Optical picture (top view) of the micro-supercapacitor after the chlorination process. The 18 interdigitated electrodes of CDC are separated by a 15-μm distance. (**E**) A 7.62-cm Si wafer containing 40 patterned micro-supercapacitors. (**F**) CV of a micro-supercapacitor in 1 M H_2SO_4 electrolyte recorded at 10 mV s^{-1}. The volumetric capacitance reaches 350 F cm^{-3}.

Fig. 4. Electrical performance. Areal-normalized Ragone plots showing the performance of several microsystems using carbon and pseudocapacitive materials in interdigitated or parallel-plate (noted with asterisks) configurations. AC, activated carbon; LSG, laser scribed graphene; OLC, onions like carbon; PANI, polyaniline; PVA, polyvinylic acetate; rGO, reduced graphene oxide; PC, polypropylene. "This work (a)" refers to 2 M EMI,BF$_4$ in AN, 4.1-μm-thick TiC film (fig. S3E), two parallel plates device. "This work (b)" refers to 2 M EMI,BF$_4$ in AN, 2.2-μm-thick TiC film, two parallel plates device (Fig. 3C). "This work (c)" refers to 1 M H_2SO_4, 1.4-μm-thick, interdigitated microdevice (Fig. 3F). Numbers in brackets are cited references.
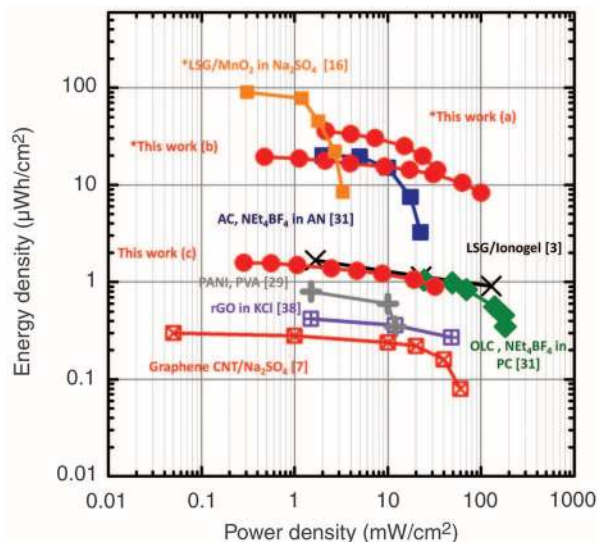
of the capacitance (180 F cm^{-3}) is still retained at 10 V s^{-1}, thus outperforming the state-of-the-art micro-supercapacitors (*1, 16, 17, 27, 29, 31*), as can be seen in the volume-normalized Ragone plot in fig. S6 showing performance of micro-supercapacitors in interdigitated and parallel-plate configurations. Because performance per device area is a key metric for the integration of electrochemical capacitors with Si-based electronics, Fig. 4 shows an area-normalized Ragone plot. Compared with other carbon-based systems, our devices show the best performance in terms of areal energy and power density in the parallel-plate configuration. Moreover, our present results obtained with carbon materials even compare favorably with thick pseudocapacitive laser-scribed graphene (LSG)/MnO$_2$ composite electrodes, achieving a very high areal capacitance of 800 mF cm^{-2}. Indeed, unlike in the present results, high areal capacitance is generally accompanied by a low-power performance because of the use of thick electrodes (*32–34*) or low areal energy and power densities because of the use
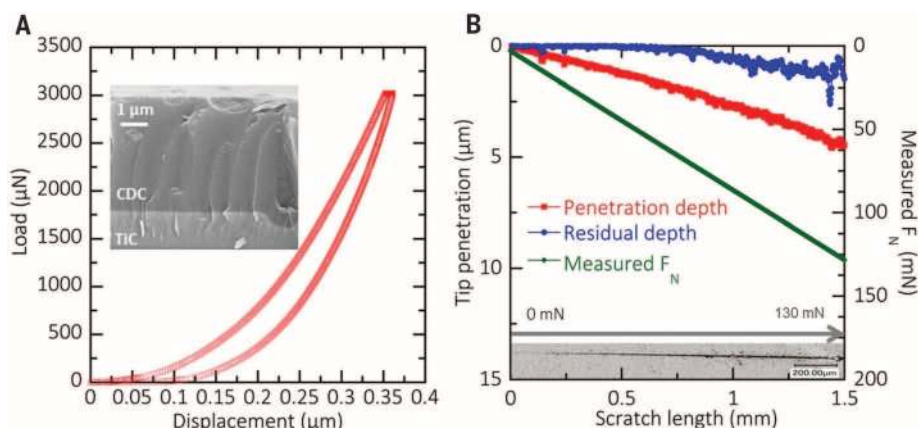
Fig. 5. Mechanical properties of the TiC/CDC layered structure. (**A**) The load versus displacement plot measured with a Berkovich nano-indenter shows more than 75% elastic recovery, with a Young's modulus of 14.5 GPa, a hardness of 1.6 GPa, and an equivalent Vickers hardness of 151 HV. (Inset) Cross section of the TiC/CDC layered structure studied. (**B**) The nano-scratch test (picture at bottom) reveals a low friction coefficient of about 0.2, which is half of that measured on TiC.

of faradic materials with a narrow operating potential window (*13*).

The mechanical properties of the films reported here differ from cracked and low-strength CDC films that frequently suffered from delamination upon cycling (*9*, *21*) or graphite, activated carbon, or nanotube films, in which particles are weakly bonded by van der Waals forces or kept together by a polymer binder (*5–7*, *31*, *35*). The load as a function of the displacement plot for a 5-μm-thick CDC film is shown in Fig. 5A, using a Berkovich indenter (supplementary materials, materials and methods). The CDC coating shows a hardness of 1.6 GPa and a Young's modulus of 14.5 GPa, which are in good agreement with literature (*36*), with a large elastic contribution (>75%) to the loading. The excellent adhesion at the TiC/CDC interface is also confirmed by the propagation of the fractures from the CDC down into the TiC layer (Fig. 5A, inset), with no crack deflection at the interface, suggesting that the CDC film has mechanical properties comparable with that of TiC (*36*).

Penetration depth during a nanoscratch test and residual depth after the test are plotted versus the distance and normal force (Fig. 5B). The delamination of the coating occurred for a normal load of 130 mN, which corresponds to a work of adhesion of 18 J m^{-2}. However, the residual depth (Fig. 5B, blue plot) remains 0 during the first 0.6 mm of the scratch tests (up to a normal force of 40 mN), giving evidence to outstanding elasticity of the porous CDC film. The friction coefficient measured during the scratch test (0.2) is twice lower on the CDC surface than on the TiC surface, highlighting the lubricating effect of the coating.

Increasing the chlorination time t_2 of the TiC film (Fig. 1A, down) leads to the separation of CDC from the Si substrate and formation of self-supported CDC films of several square centimeters in area (fig. S7, A and B). The CV at 20 mV s^{-1} in a 1 M H_2SO_4 electrolyte is shown in fig. S7C.

Similarly to the partially chlorinated films, a high capacitance of 180 mF cm^{-2} (300 F cm^{-3}) was obtained. By tuning the pressure in the chamber during the TiC deposition process (0.001 mbar) and the chlorination temperature (350°C), internal stress in 3-μm-thick TiC films led to CDC rolls (Fig. 1E). Such rolling has been observed for CVD semiconductor films (*37*). A TEM image of the film (fig. S7D) shows its amorphous structure. The excellent mechanical properties as well as the absence of large pores or cracks (Figs. 1B and 2C), which would act as defects that weaken the film, may be responsible for the observed film integrity after separation. X-ray photoelectron spectroscopy (XPS) analysis shows that the free-standing films have similar composition from the film surface to the bulk (Fig. S7, E and F). Another key feature is the possibility offered by these freestanding CDC films to be transferred onto flexible substrates, as shown in fig. S8, A and B. The electrochemical performance of a 8-μm-thick CDC film transferred onto a flexible polyethylene terephthalate substrate reached 240 mF cm^{-2} (300 F cm^{-3}) in the 1 M H_2SO_4 electrolyte. Additionally, freestanding patterned CDC microelectrodes could also be prepared from the full chlorination of patterned TiC (fig. S7G), which is promising for further development of high-performance stand-alone supercapacitors that could be used in flexible or wearable applications.

REFERENCES AND NOTES

1. M. Beidaghi, Y. Gogotsi, *Energy Environ. Sci.* **7**, 867–884 (2014).
2. P. Simon, Y. Gogotsi, *Nat. Mater.* **7**, 845–854 (2008).
3. M. F. El-Kady, R. B. Kaner, *Nat. Commun.* **4**, 1475 (2013).
4. Z. Peng, J. Lin, R. Ye, E. L. G. Samuel, J. M. Tour, *ACS Appl. Mater. Interfaces* **7**, 3414–3419 (2015).
5. M. F. El-Kady, V. Strong, S. Dubin, R. B. Kaner, *Science* **335**, 1326–1330 (2012).
6. B. Hsia *et al.*, *Nanotechnology* **25**, 055401 (2014).
7. J. Lin *et al.*, *Nano Lett.* **13**, 72–78 (2013).
8. J. Chmiola, C. Largeot, P. L. Taberna, P. Simon, Y. Gogotsi, *Science* **328**, 480–483 (2010).
9. P. Huang *et al.*, *J. Power Sources* **225**, 240–244 (2013).
10. E. Eustache *et al.*, *Electrochem. Commun.* **28**, 104–106 (2013).
11. X. Wang, Y. Yin, X. Li, Z. You, *J. Power Sources* **252**, 64–72 (2014).
12. M. S. Kim, B. Hsia, C. Carraro, R. Maboudian, *Carbon* **74**, 163–169 (2014).
13. C. Guan *et al.*, *Nanotechnology* **26**, 094001 (2015).
14. R. Warren, F. Sammoura, F. Tounsi, M. Sanghadasa, L. Lin, *J. Mat. Chem. A* **3**, 15568–15575 (2015).
15. J. J. Yoo *et al.*, *Nano Lett.* **11**, 1423–1427 (2011).
16. M. F. El-Kady *et al.*, *Proc. Natl. Acad. Sci. U.S.A.* **112**, 4233–4238 (2015).
17. X. Wang *et al.*, *Nanoscale* **5**, 4119–4122 (2013).
18. C. Shen *et al.*, *J. Power Sources* **234**, 302–309 (2013).
19. Z.-S. Wu *et al.*, *Adv. Mater.* **27**, 4054–4061 (2015).
20. T. M. Dinh *et al.*, *Nano Energy* **10**, 288–294 (2014).
21. M. Heon *et al.*, *Energy Environ. Sci.* **4**, 135–138 (2011).
22. J. Chmiola *et al.*, *Science* **313**, 1760–1763 (2006).
23. B. H. Lohse, A. Calka, D. Wexler, *J. Alloys Compd.* **434–435**, 405–409 (2007).
24. F. Béguin *et al.*, *Electrochim. Acta* **51**, 2161–2167 (2006).
25. Y. Gogotsi, P. Simon, *Science* **334**, 917–918 (2011).
26. C. Zhang, W. Lv, Y. Tao, Q.-H. Yang, *Energy Environ. Sci.* **8**, 1390–1403 (2015).
27. L. Wei, N. Nitta, G. Yushin, *ACS Nano* **7**, 6498–6506 (2013).
28. Y. Tao *et al.*, *Sci. Rep.* **3**, 2975 (2013).
29. C. Z. Meng, J. Maeng, S. W. M. John, P. P. Irazoqui, *Adv. Energy Mater.* **4**, 1301269 (2014).
30. S. Li, X. Wang, H. Xing, C. Shen, *J. Micromech. Microeng.* **23**, 114013 (2013).
31. D. Pech *et al.*, *Nat. Nanotechnol.* **5**, 651–654 (2010).
32. G. Xiong, C. Meng, R. G. Reifenberger, P. P. Irazoqui, T. S. Fisher, *Electroanalysis* **26**, 30–51 (2014).
33. B. Dunn, J. W. Long, *Electrochem. Soc. Interface* **17**, 49 (2008).
34. A. Ferris, S. Garbarino, D. Guay, D. Pech, *Adv. Mater.* **27**, 6625–6629 (2015).
35. M. Beidaghi, C. L. Wang, *Electrochim. Acta* **56**, 9508–9514 (2011).
36. Y. Gogotsi, S. Welz, D. A. Ersoy, M. J. McNallan, *Nature* **411**, 283–287 (2001).
37. V. Y. Prinz, *Microelectron. Eng.* **69**, 466–475 (2003).
38. M. Beidaghi, C. L. Wang, *Adv. Funct. Mater.* **22**, 4501–4510 (2012).

SUPPLEMENTARY MATERIALS

www.sciencemag.org/content/351/6274/691/suppl/DC1
Materials and Methods
Supplementary Text
Figs. S1 to S8
Tables S1 and S2
References (*39–51*)